The Astrophysical Journal, 997:151 (14pp), 2026 February 1 https://doi.org/10.3847/1538-4357/ae1f0b
© 2026. The Author(s). Published by the American Astronomical Society.
OPEN ACCESS

Explaining the Origin of TeV Gamma Rays from M87 during High and Low States

Nibedita Mondal[1], Sandeep Kumar Mondal[2], and Nayantara Gupta[1]
[1] Astronomy & Astrophysics Group, Raman Research Institute, Sadashivanagar, Bangalore 560080, Karnataka, India; mon.nibe.mcc@gmail.com
[2] Tsung-Dao Lee Institute, Shanghai Jiao Tong University, 1 Lisuo Road, Shanghai 201210, People's Republic of China; sandeep@sjtu.edu.cn
Received 2025 September 1; revised 2025 November 2; accepted 2025 November 7; published 2026 January 20

Abstract

The detection of very-high-energy gamma rays from M87 can provide crucial insights into particle acceleration and radiation mechanisms in jets. The recent observations by the Large High Altitude Air Shower Observatory detector extend the energy range of TeV gamma-ray astronomy, and also the variability study to the TeV energy domain. We have modeled the low state and flare state multiwavelength spectral energy distributions of M87 within a time-dependent framework. In our model, the low state gamma-ray flux results from the emissions from the subparsec and the kiloparsec scale jets of M87, whereas the flare state gamma-ray flux is mainly produced in the subparsec scale jet. We have shown that the spectral and temporal features of the TeV gamma-ray spectrum of M87 are consistent with this two-zone model, where the contribution from the subparsec scale jet significantly increases during the flare state.

Unified Astronomy Thesaurus concepts: High energy astrophysics (739); Gamma-ray astronomy (628); Active galactic nuclei (16)

1. Introduction

M87 is also known as 4FGL J1230.8+1223, NGC 4486, or 3C274, and commonly categorized as a Fanaroff–Riley I radio galaxy (B. L. Fanaroff & J. M. Riley 1974) located at redshift $z = 0.00428$ (M. Cappellari et al. 2011) with R.A. $= 187.^{\circ}7059$ and decl. $= 12.^{\circ}3911$.

It is well known as one of the brightest radio sources in the sky since the beginning of radio astronomy (J. G. Bolton et al. 1949). The large-scale radio structure of this galaxy extends up to 80 kpc (B. Y. Mills 1952). The recent review paper by K. Hada et al. (2024) gives an excellent overview of different aspects of this source.

It is one of the nearest radio galaxies and has been identified as a very-high-energy (VHE) gamma-ray emitter in the TeV energy range. Since M87 is the only source that has been traced from the supermassive black hole (SMBH) shadow at about 0.005 pc (Event Horizon Telescope Collaboration 2019a, 2019b, 2019c, 2019d, 2019e, 2019f) to the outer jet extending to ∼25 kpc, exhibiting a relativistic jet, it has been considered to be the best-researched laboratory for studying SMBH physics, accretion, and radio-loud active galactic nuclei (AGN) properties.

M87 exhibits brightness across the entire electromagnetic spectrum, which makes it an excellent candidate for broadband multiwavelength observations. Multiwavelength studies at different epochs reported emission across timescales from days to years, but due to insufficient data in different time domains, the underlying physics of temporal variations remains unclear (K. Hada et al. 2024).

VHE ($0.1 \sim 100$ TeV) gamma rays are messengers of cosmic-ray acceleration sites. The origin of this VHE emission of jetted AGNs like M87 is still elusive. The High-Energy-Gamma-Ray Astronomy reported the first VHE gamma-ray emission from M87 in 1998–1999 (F. Aharonian et al. 2003). Furthermore, the next-generation high-energy instruments such as High Energy Stereoscopic System (H.E.S.S.; F. Aharonian et al. 2006), Very Energetic Radiation Imaging Telescope Array System (VERITAS; V. A. Acciari et al. 2008), Major Atmospheric Gamma Imaging Cherenkov (MAGIC; J. Albert et al. 2008), and Fermi Large Area Telescope (Fermi-LAT; A. A. Abdo et al. 2009) also reported gamma-ray emission. Additionally, the High Altitude Water Cherenkov (HAWC) observatory recorded long-term VHE emission from this source at a weak statistical significance (3.6σ; A. Albert et al. 2021). According to previous studies (F. Aharonian et al. 2006; J. Albert et al. 2008; E. Aliu et al. 2012), M87 not only exhibits variations in its spectrum and flux in flaring states but also displays complex behavior in nonflaring states at gamma-ray frequencies (F. Ait Benkhali et al. 2019). The following is a brief history of M87 in different activity states.

Four significant VHE flares have been detected in 2005, 2008, 2010, and 2018 (F. Aharonian et al. 2006; J. Albert et al. 2008; A. Abramowski et al. 2012; J. C. Algaba et al. 2024), exhibiting 1 day variability. Large High Altitude Air Shower Observatory (LHAASO) detected a VHE flux state (Z. Cao et al. 2024) in 2022 for 8 days. Apart from these, the source has been seen in the quiescent state, with a high flux state occasionally appearing for very short timescales.

During long-term monitoring from 2021 to 2024, LHAASO observed M87 with a statistical significance of $\sim 9\sigma$, and the observed energy spectrum extended up to 20 TeV (Z. Cao et al. 2024). The HAWC reported the emission from M87 over approximately 7.5 yr (from 2015 to 2022) in the energy range of 16–26 TeV (R. Alfaro et al. 2025).

In this work, we have studied the jet emission from M87 with data analysis and modeling of the spectral energy distributions (SEDs) to address the key aspects of jet physics, in particular, the emission mechanisms and regions in the high-energy regime, in light of the gamma-ray data recently reported by the LHAASO observatory.

The Fermi-LAT data analysis has been discussed, and the possibility of a GeV flare in Fermi-LAT data has been explained in Section 2. Subsequently, the Swift X-ray Telescope (XRT) and Ultraviolet/Optical Telescope (UVOT) data analysis have been discussed, and the LHAASO data, the other archival data used in this study, have been mentioned in this section. Section 3 is on the modeling of the SED covering the multiwavelength observations, and our results are

Original content from this work may be used under the terms of the Creative Commons Attribution 4.0 licence. Any further distribution of this work must maintain attribution to the author(s) and the title of the work, journal citation and DOI.

mentioned in Section 4. The discussion and conclusion are presented in Section 5.

2. Multiwavelength Data Accumulation

2.1. Fermi-LAT Data Analysis

The Fermi Gamma-ray Space Telescope is a space-based high-energy gamma-ray observatory. It carries two instruments: the LAT, which serves as the primary instrument, and the Gamma-ray Burst Monitor. The LAT is an imaging, pair-conversion, wide-field-of-view telescope, which can detect gamma rays in the energy range from 20 MeV to beyond 300 GeV, with a field of view of 2.7 sr at 1 GeV and above (W. B. Atwood et al. 2009). It scans the entire sky every 3 hr and has been in continuous operation since 2008 August.

For our work, we conducted a comprehensive analysis of Fermi-LAT gamma-ray Pass 8 data for M87, using data collected from the Fermi Science Support Center server (Fermi Science Support Center 2025), covering more than 16.5 yr (2008 August 4–2025 February 6). The data were extracted from a circular region of a radius 30°, centered on M87, covering the energy range 0.1–100 GeV.

The dataset was processed using Fermipy (v1.0.1; M. Wood et al. (2017)), an open-source Python package for Fermi-LAT data analysis. A 15° × 15° region was defined in the configuration file, and only photons with energies between 0.1 and 100 GeV were included, while events with zenith angles above 90° were excluded to reduce contamination from the Earth's limb. For event selection, the "P8R3 SOURCE" class (evclass = 128) was used, as recommended for analyses with relatively small regions of interest (ROIs) less than 25° (P. Bruel et al. 2018). The evtype parameter was set to 3 to include all event types, covering both the front and back sections of the tracker. Data quality cuts were applied using `DATA_QUAL` > 0 && `LAT_CONFIG` == 1 to ensure that only high-quality data collected under standard LAT science operations were included.

For source modeling, the Fermi-LAT Fourth Source Catalogue Data Release 4 (4FGL-DR4; gll_psc_v35.fits; J. Ballet et al. 2023) was included, with the Galactic diffuse emission modeled using the gll_iem_v07 template (F. Acero et al. 2016) and the isotropic extragalactic background modeled with iso_p8r3_source_v3_v1.txt. Within the ROI, the parameters of 4FGL J1230.8+1223, together with the isotropic (isodiff) and Galactic diffuse (galdiff) components, were left free. The normalization (norm) of the diffuse components was allowed to vary, while for 4FGL J1230.8 +1223, represented by a log-parabola, the norm, spectral index (alpha), and curvature (beta) were freed. The fit was performed using `gta.fit()` with the NEWMINUIT optimizer, iterating until the fit quality reached 3 to obtain the best-fit model.

The Fermi-LAT data analysis has two objectives: (i) gamma-ray SED analysis and (ii) light-curve analysis to investigate a potential GeV flare coinciding with the VHE flare from M87 in 2022.

LHAASO monitored M87 from MJD 59281–60385 (Z. Cao et al. 2024); the details are given in Table 1. Considering this timeline, we have analyzed the Fermi-LAT gamma-ray SED for three states (low-state 1, flare state, low-state 2), using `gta.sed()` in Fermipy.

Following Fermipy documentation (Fermipy Collaboration 2016), the Fermi-LAT gamma-ray light curve of M87 was then extracted in different time bins, as described in Section 2.1.3.

Table 1
Time Intervals of Different States of M87 between 2021 and 2024 (MJD 59281–60385), Based on LHAASO Observation Z. Cao et al. (2024)

Time Interval (MJD)	State
59281–59607	Preflare (low-state 1 or LS1)
59607–59615	Flare State
59615–60385	Postflare (low-state 2 or LS2)

2.1.1. Gamma Ray: Likelihood Test Using Different Spectral Model

Fermi-LAT data analysis incorporates the maximum likelihood (ML) method to determine the best-fit model of the SED data. We considered two spectral models : (i) PowerLaw (PL), and (ii) LogParabola (LP) for comparison.[3]

1. PowerLaw (PL):

$$\frac{dN}{dE} = N_{\rm PL}\left(\frac{E}{E_\circ}\right)^{-\alpha}, \quad (1)$$

where $N_{\rm PL}$ is the normalization factor, $E_\circ$ is the scaling factor or `pivot energy`, and α is the spectral index of the PL model. $N_{\rm PL}$ and α were kept free during this model fitting. The 4FGL catalog assigns a `pivot energy` $E_\circ$ to each source, which is the point at which the fit parameters have the least correlation and the spectrum is well measured. In our analysis, the scaling factor or pivot energy is fixed at its catalog value of 1.14 GeV (J. Ballet et al. 2023) for both the PL and LP spectral models.

2. LogParabola (LP): The LP model is widely used in gamma-ray astronomy, accounts for spectrum curvature, and is parameterized as follows:

$$\frac{dN}{dE} = N_{\rm LP}\left(\frac{E}{E_\circ}\right)^{-\alpha+\beta\log(E/E_\circ))}, \quad (2)$$

where $N_{\rm LP}$ is the prefactor, the photon index α, and β is the curvature index. $N_{\rm LP}$, α, and β are considered free parameters during fitting.

Table 2 shows the best-fit parameters from the likelihood analysis, where the LP model best describes the gamma-ray spectrum in the flare and low states.

2.1.2. Gamma-Ray Spectral Analysis Outcomes

1. Preflare state (low-state 1 or LS1): The source (4FGL J1230.8+1223) is detected with statistical significance TS = 159.92 from our likelihood analysis. The gamma-ray spectrum for the preflare state is well represented by a log-parabola model with $\alpha = 2.026 \pm 0.003$, $\beta = 0.073 \pm 0.001$. and corresponding integrated flux over 0.1–100 GeV of 1.723 ($\pm$ 0.001) $\times 10^{-8}$ ph cm^{-2} s^{-1}.

[3] https://fermi.gsfc.nasa.gov/ssc/data/analysis/scitools/source_models.html

Table 2
Results of Fermi-LAT SEDs of Different States, Fitted with Different Spectral Models: PL and LP

	PowerLaw (PL)					
State	$F_{0.1-100\ \mathrm{GeV}}$ (10^{-8} ph cm^{-2} s^{-1})	Index (Γ)	Test Statistics (TS)	$-$log(Likelihood)		
Preflare (LS1)	2.028 ± 0.009	2.080 ± 0.002	158.06	102,802.22		
Flare	3.02 ± 1.46	2.23 ± 0.22	2.55	5278.21		
Postflare (LS2)	1.36 ± 0.21	1.95 ± 0.07	307.11	176,206.73		
	LogParabola (LP)					
State	$F_{0.1-100\ \mathrm{GeV}}$ (10^{-8} ph cm^{-2} s^{-1})	α	β	TS	$-$log(Likelihood)	Δ log(Likelihood)
Preflare (LS1)	*1.723 ± 0.001*	*2.026 ± 0.003*	*0.073 ± 0.001*	*159.92*	*102,801.82*	*-0.40*
Flare	*1.39 ± 0.42*	*3.33 ± 0.34*	*1.84 ± 0.24*	*5.84*	*5276.69*	*-1.52*
Postflare (LS2)	*0.94 ± 0.23*	*1.79 ± 0.12*	*0.14 ± 0.06*	*312.38*	*176,203.38*	*-3.35*

Note. Model preference is determined using the log-likelihood ratio test, where $\Delta\log(\mathrm{Likelihood}) = \log(\mathrm{Likelihood})_{\mathrm{LP}} - \log(\mathrm{Likelihood})_{\mathrm{PL}}$. The tabulated values appear negative because they are derived from $-\log(\mathrm{Likelihood})$, a smaller $-\log(\mathrm{Likelihood})$ (or equivalently, a larger $\log(\mathrm{Likelihood})$) corresponds to a better fit. Therefore, the negative $\Delta\log(\mathrm{Likelihood})$ values indicate that the LogParabola (LP) model yields higher likelihoods than the PowerLaw (PL) model and thus provides the statistically preferred fit in all activity states. The $\Delta\log(\mathrm{Likelihood})$ values of the best-fitted models are highlighted in italic font.

2. Flare state: In this state, the gamma-ray spectrum is defined by a log-parabola with $\alpha = 3.33 \pm 0.34$ and $\beta = 1.84 \pm 0.24$, detected with TS = 5.84. An integrated flux of $1.39\ (\pm 0.42) \times 10^{-8}$ ph cm^{-2} s^{-1} over 0.1–100 GeV is obtained.
3. Postflare state (low-state 2 or LS2): The log-likelihood test for the postflare state signifies that a log-parabola model is a better representation than a single power-law model with an integrated flux of $0.94\ (\pm 0.23) \times 10^{-8}$ ph cm^{-2} s^{-1} over the energy range 0.1–100 GeV with best-fit indices $\alpha = 1.79 \pm 0.12$ and $\beta = 0.14 \pm 0.06$. The source is detected with high statistical significance, TS = 312.38, compared to other states.

2.1.3. GeV Flare in Fermi-LAT

We examined the possibility of a GeV flare in Fermi-LAT coincident with the VHE flaring period detected by LHAASO in 2022 (Z. Cao et al. 2024) by analyzing the Fermi-LAT gamma-ray light curve over 16.5 yr, from 2008 August 4 to 2025 February 6 (MJD 54682.65-60712.00) using 30 day bins. The Bayesian block method (J. D. Scargle et al. 2013) was applied to identify flux enhancements (Figure 1(a)). A horizontal maroon color dashed line indicates the average gamma-ray flux over the full period, while the Bayesian blocks are shown as a black solid line. The orange-shaded region highlights the interval during which LHAASO continuously monitored the source (MJD 59281–60385; Z. Cao et al. 2024).

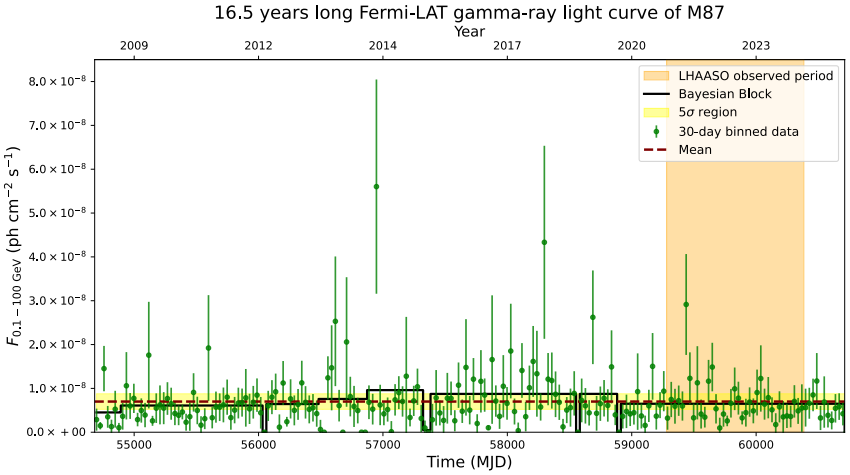
Statistically, no flux-enhanced state was detected during the LHAASO monitored period, i.e., MJD 59281–60385. There is a possibility that the flux may have increased slightly compared to the average gamma-ray flux between 2014 and 2019; however, this period falls outside the focus of our study.

Typically, after identifying flux enhancements in a light curve with larger time bins, we analyze the light curve with shorter binning to reveal possible substructures more clearly (S. K. Mondal et al. 2021). In this case, we followed Z. Cao et al. (2024) and further analyzed this 3 yr Fermi-LAT data (MJD 59281–60385) in 90 day bins (Figure 1(b)), marking the LHAASO-detected VHE flare with a gray-shaded region. From Figure 1(b), it can be seen that the source is not in a high-flux state in the MeV–GeV band, and the 90 day binned data have large flux uncertainties. These errors would increase further if we analyze the light curve in smaller time bins. To demonstrate this, we analyzed the same Fermi-LAT light curve using 7 day binning (Figure 1(c)). The flux variation appears highly random, and the flux errors are very large. Using the Bayesian block method, we did not find any GeV flaring during the VHE flare (gray-shaded region), and the data quality is not feasible for further analysis in smaller time bins (S. K. Mondal et al. 2023). Finally, we analyzed the ∼60 day light curve in 8 day bins (Figure 1(d)), as also done in Z. Cao et al. (2024). Only one data point falls within the VHE flare period (gray-shaded region), with TS > 25. Because only a single data point is available for this period and flux uncertainties increase when using smaller time bins, it is not possible to reliably determine whether Fermi-LAT detected a flare coincident with the VHE event observed by LHAASO in 2022. Given this limitation, any claim of a flare state would be statistically unsupported. Reduced flux uncertainties would have allowed finer temporal binning and a more detailed examination of the light curve for potential flux enhancements. Therefore, the current Fermi-LAT data do not provide statistically significant evidence for a GeV flaring event coincident with the VHE flare of M87.

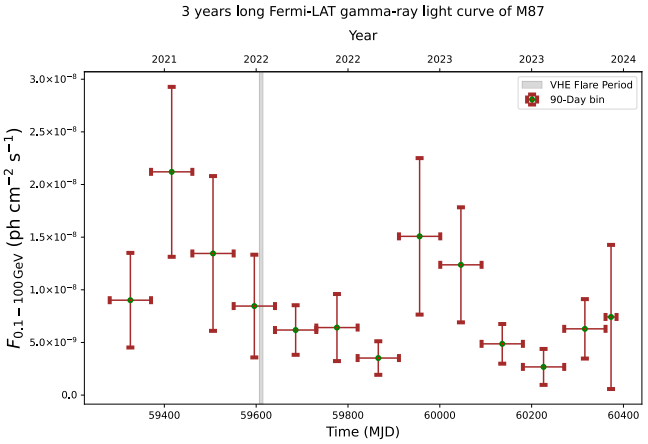
2.2. Swift XRT and UVOT Data Analysis

The Neil Gehrels Swift is a multiwavelength space-based observatory with three instruments onboard: Burst Alert Telescope (15–150 keV), XRT (0.3–10 keV), and UVOT (170–600 nm) (D. N. Burrows et al. 2005). It observes the sky in hard X-ray, soft X-ray, ultraviolet, and optical wave bands. Swift observations of M87 were retrieved from the Swift Master Catalog (swiftmastr) using the HEASARC Xamin interface.[4] We searched for observations centered on M87 by

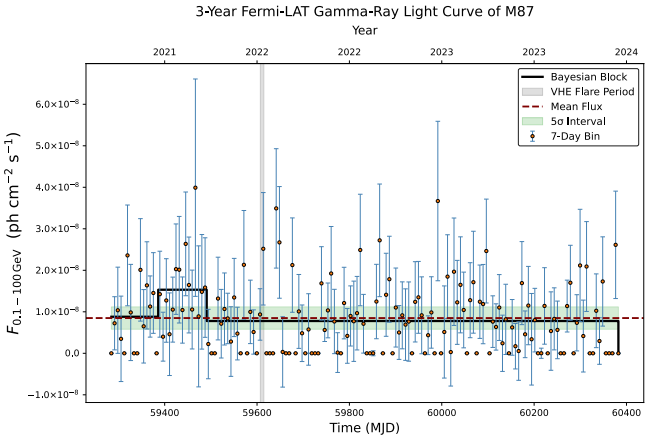
[4] https://heasarc.gsfc.nasa.gov/xamin/



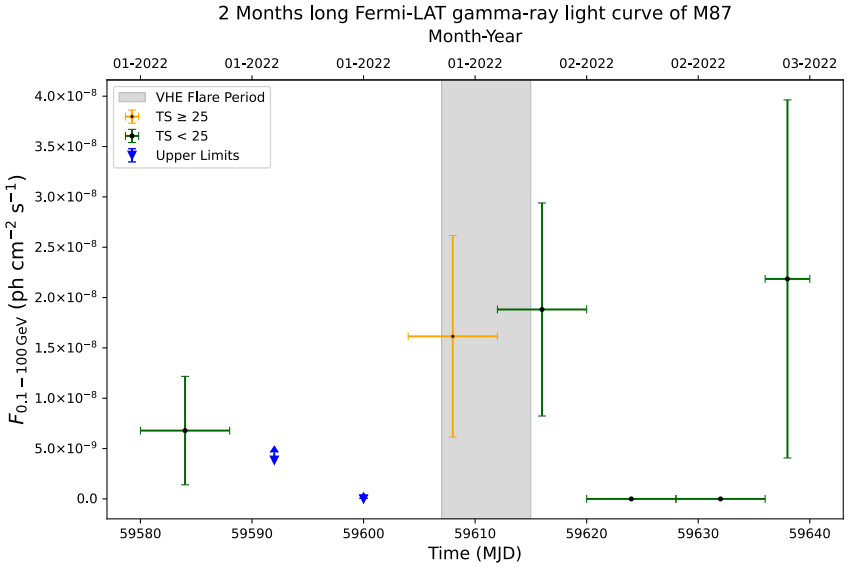
(a) 16.5-year (MJD 54682–60712) long 30-day binned light curve of M87. Orange shaded region: period of continuous LHAASO monitoring (Cao et al. 2024).



(b) 3-year (MJD 59281–60385) 90-day binned light curve.



(c) 3-year (MJD 59281–60385) 7-day binned light curve.



(d) 2-month-long 8-day binned light curve of M87.

Figure 1. Gamma-ray light curves of M87 observed with Fermi-LAT at different time binning.

querying the catalog with the source name "M87" (J2000 position: R.A. = 187.°7059, decl. = +12.°3911). The default Xamin search parameters were used, corresponding to a circular search radius of 0.°1. We found 54 Swit-XRT/UVOT observations for the period MJD 59281 and 60385. Observations that yielded statistically insignificant data were excluded

Table 3
Discarded Swift-XRT and UVOT Observations of M87

Sr. No.	Observation ID	Instrument	Starting Time (MJD)	XRT Exposure (ks)	UVOT Exposure (ks)
1	00031105075[a]	SWIFT-XRT/UVOT	59307.253	0.9	0.9
2	00031105076[a]	SWIFT-XRT/UVOT	59310.239	0.9	0.9
3	00031105078[a]	SWIFT-XRT/UVOT	59315.143	0.6	0.6
4	00031105083[b]	SWIFT-XRT/UVOT	59310.005	0.01	0.0
5	00031105093[a]	SWIFT-XRT/UVOT	60048.201	0.8	0.8
6	00031105094[a]	SWIFT-XRT/UVOT	60051.318	0.9	0.9
7	00096453001[a]	SWIFT-XRT/UVOT	59650.352	1.0	1.0
8	00096453003[a]	SWIFT-XRT/UVOT	59652.167	0.7	0.7
9	00096453008[a]	SWIFT-XRT/UVOT	59658.257	0.6	0.6
10	00096453009[a]	SWIFT-XRT/UVOT	59659.443	0.7	0.7
11	00096453011[a]	SWIFT-XRT/UVOT	59661.234	0.8	0.8
12	00096453012[a]	SWIFT-XRT/UVOT	59662.498	0.9	0.9
13	00096453013[a]	SWIFT-XRT/UVOT	59663.178	0.6	0.6
14	00096453014[a]	SWIFT-XRT/UVOT	59664.700	0.9	0.9
15	00096453016[a]	SWIFT-XRT/UVOT	59666.410	0.7	0.7
16	00096453028[a]	SWIFT-XRT/UVOT	59677.353	0.7	0.7

Notes.
[a] Excluded only from Swift-XRT analysis.
[b] Excluded from both Swift-XRT and UVOT analyses.

from the analysis. The discarded ObsIDs are listed in Table 3. No observations were found corresponding to the 8 day VHE flare (MJD 59607–59615), i.e., all the Swift observations correspond to LS1 and LS2.

We followed the standard data reduction procedure[5] to prepare the raw data, i.e., Level 1 data for analysis, using the software package, HEASoft.[6] `Xrtpipeline` (v0.13.5) has been used to generate the cleaned event files corresponding to each observation. During the analysis, the calibration file (CALDB; version 20240522) and other standard screening criteria have been applied to the cleaned data. We have used the photon count (PC) mode data for our analysis. For nonpiled-up spectra, we consider a circular source region between 32″ and 40″, with the source at the center. In case of the piled-up spectra, we carried out the standard procedure for pile-up correction,[7] and an annular source region centered on the source has been considered. In both cases, the background was extracted from a circular region located far from the source of interest, in an area with minimal contamination from other sources, and with a radius twice that of the source region. Using the `xselect` tool, we defined the source and background regions and extracted the corresponding spectrum files for each observation. `xrtmkarf` and `grppha` programs were utilized to create an ancillary response file and group the spectrum file with its corresponding response matrix file. Then, `Addspec` and `mathpha` were employed.

In this work, we produced the combined source and background spectra separately for each of the two low states, LS1 and LS2. As mentioned earlier, the "flare" state does not have any simultaneous Swift observation. LS1 comprises 11 observations acquired between 2021 March 19 and 2022 January 11, and LS2 consists of 26 observations from 2022 March 12 to 2023 April 23.

In the next step, we again used `grppha` to group the combined source and background files of each state and generate the final spectrum file, which was then used in `xspec` for further analysis.

The spectra of the two low states were modeled using the `xspec` package (K. A. Arnaud 1996; Version 12.14.1). We found that both Swift-XRT low state spectra are best described by the `mekal`[8] + (TBabs[9]*PL[10]) model (S. Connolly et al. 2016), providing a better fit than mekal + (TBabs*logpar[11]) or mekal + (TBabs*plec[12]). The best-fit parameters were derived using chi-square statistics. Table 4 summarizes the free and fixed parameter values of the best-fit model. Other than these parameters, the normalization factors for both the mekal and PL components are left free. Finally, we extracted the unabsorbed spectra corresponding to LS1 and LS2, which were then used in constructing the multiwavelength SEDs (MWSEDs) of M87 for these two states.

M87 was also monitored by the Swift UVOT (P. W. Roming et al. 2005) with six filters: v (5468 Å), b (4392 Å), u (3465 Å), uvw1 (2600 Å), uvm2 (2246 Å), and uvw2 (1928 Å), at the same time with Swift-XRT. In LS1, the number of observations is 10, 8, and 11 for the v, b, and u bands, respectively, and 10, 11, and 10 for uvw1, uvm2, and uvw2. For LS2, the optical bands have 8 (v), 9 (b), and 16 (u) observations, while the UV bands include 16 (uvw1), 17 (uvm2), and 16 (uvw2) observations. For the extraction of the source region from the Swift-UVOT data, a circular region of radius 5″ was considered, and for the background region, a

[5] https://www.swift.ac.uk/analysis/index.php
[6] https://heasarc.gsfc.nasa.gov/docs/software/heasoft/
[7] https://www.swift.ac.uk/analysis/xrt/pileup.php
[8] https://heasarc.gsfc.nasa.gov/docs/software/xspec/manual/node199.html
[9] https://heasarc.gsfc.nasa.gov/docs/software/xspec/manual/node283.html
[10] https://heasarc.gsfc.nasa.gov/docs/software/xspec/manual/node222.html
[11] https://heasarc.gsfc.nasa.gov/docs/software/xspec/manual/node196.html
[12] https://heasarc.gsfc.nasa.gov/docs/software/xspec/manual/node163.html

Table 4
Swift-XRT Model Parameter Values for Preflare (LS1) and Postflare (LS2)

State	Parameters	Values	χ^2(Degrees of Freedom)
LS1	Plasma temperature (keV)	$1.58^{+0.05}_{-0.05}$	92.49(91)
	n_H[a] (cm^{-3})	1[b]	
	Abundance[a]	1	
	Redshift[a]	0.00428	
	Switch[a]	2[c]	
	N_H[a] (cm^{-2})	0.45×10^{-22}[d]	
	Spectral index	$1.92^{+0.76}_{-0.76}$	
LS2	Plasma temperature (keV)	$1.42^{+0.03}_{-0.03}$	155.38(119)
	n_H[a] (cm^{-3})	1[b]	
	Abundance[a]	1	
	Redshift[a]	0.00428	
	Switch[a]	2[c]	
	N_H[a] (cm^{-2})	0.45×10^{-22}[d]	
	Spectral index	$2.94^{+0.32}_{-0.32}$	

Notes.
[a] Denotes that the parameter is fixed.
[b] Adopted from D. A. Leahy et al. (2024).
[c] For using the updated APEC model.
[d] Denotes the parameter value is taken from S. Connolly et al. (2016).

circle of radius 15″ was taken, located far away from the source. We have summed all exposures corresponding to a particular energy band using `uvotimsum`. Then, the "uvotsource" tool has been used to extract the magnitude of the source. This magnitude has been corrected to account for galactic absorption. To obtain the extinction values (A_λ) for each Swift-UVOT filter, the Python package `extinction`[13] was utilized. We have considered the E. L. Fitzpatrick (1999) dust extinction function with $R_V = 3.1$, where R_V is the slope of the extinction curve. For the diffuse interstellar medium (ISM), this corresponds to a visual extinction $A_V = 0.0612$ mag and reddening $E(B-V) = 0.0197$ mag (E. F. Schlafly & D. P. Finkbeiner 2011), consistent with the average ISM value of $R_V = 3.1$ (G. V. Schultz & W. Wiemer 1975; D. C. B. Whittet & I. G. van Breda 1980; G. H. Rieke & M. J. Lebofsky 1985). The intrinsic magnitude ($M_{\rm in}$), the extinction parameter (A_λ), and the observed magnitude of the source ($M_{\rm obs}$) are related as follows $M_{\rm in} = M_{\rm obs} - A_\lambda$. We have calculated the intrinsic source flux using this relation $M_{\rm in} = -2.5\log_{10}(\text{Flux}) - \text{Zero}$ point. The zero-point is a calibration parameter that defines the reference count rate corresponding to a standard X-ray flux for each detector mode and energy band in Swift XRT. It allows conversion of raw PC rates into physically calibrated fluxes or luminosities. Zero-points are empirically determined from observations of an X-ray standard source with well-characterized spectra. And finally, we calculated the Swift-UVOT SED of LS1 and LS2 and used it to construct the MWSED of the low state. In Table 5, we have reported the fluxes for the different optical-UV bands from Swift observations of M87, which also lists the band name, wavelength, $M_{\rm in}$, A_λ, $M_{\rm in}$, and zero-point. The zero-point values are taken from A. A. Breeveld et al. (2011).

[13] https://extinction.readthedocs.io/en/latest/

2.3. Archival Data

In this work, we have used the archival data from LHAASO, Monitoring of Jets in Active Galactic Nuclei with VLBA Experiments (MOJAVE), Markarian Multiwavelength Data Center (MMDC), and Space Science Data Centre (SSDC).

2.3.1. LHAASO Data

The LHAASO (Z. Cao 2010) is a next-generation ground-based facility in Daocheng, China, designed to investigate the origin of cosmic rays and the mechanisms of VHE gamma-ray production over an extensive energy range from ∼100 GeV to 1 EeV. It consists of three major detector systems: the Water Cherenkov Detector Array (WCDA; H.-C. Li et al. 2014), optimized for gamma-ray observations in the 100 GeV–30 TeV range; the Kilometer Square Array (KM2A), operating in the 30 TeV–1 PeV range for precise cosmic-ray composition studies (S. Cui et al. 2014; F. Aharonian et al. 2021); and the Wide Field-of-View Cherenkov Telescope Array (S. Zhang et al. 2020), for cosmic-ray physics from 10 TeV to 1 EeV. We have used the simultaneous gamma-ray data from the low state and flare state, collected by LHAASO-WCDA (2021 March 8–2024 March 16) and LHAASO-KM2A (2021 July 20–2024 January 31) from Z. Cao et al. (2024).

2.3.2. MOJAVE Data

The MOJAVE is a long-term program to monitor radio brightness and polarization in AGN jets across the northern sky at 15 GHz (MOJAVEWebpage 2016). With an angular resolution of greater than 1 mas, MOJAVE captures a full polarization image by monitoring at these wavelengths: 7 mm, 1.3 cm, and 2 cm. We utilized simultaneous data from MOJAVE.[14] We have used one dataset for LS1, collected on 2021 May 1, and four datasets for LS2, spanning from 2022 March 18 to 2024 January 28, from the MOJAVE/2 cm Survey Data Archive to build the MWSED. No simultaneous MOJAVE data has been found that corresponds to the flare state.

2.3.3. MMDC Data

The MMDC[15] (D. Bégué et al. 2024; N. Sahakyan et al. 2024a, 2024b) is a web-based tool designed to build and analyze multiwavelength data from blazars. In our work, we have collected multiwavelength data from MMDC, which includes (i) optical data from the All-Sky Automated Survey for Supernovae (ASAS-SN) and (ii) infrared data from the Near-Earth Object Wide-field Infrared Survey Explorer (NEOWISE) and the Zwicky Transient Facility (ZTF) for both LS1 and LS2. For the flare state, we have only found simultaneous optical data collected from ASAS-SN.

2.3.4. SSDC Data

We gathered multiwavelength data from SSDC SED Builder,[16] which are displayed in Figures 2, 3, 4, and 5 as gray circles.

2.3.5. Other Data Sources

We collected nonsimultaneous data from various observational facilities, listed in Table 6.

[14] https://www.cv.nrao.edu/MOJAVE/sourcepages/1228+126.shtml
[15] https://mmdc.am/
[16] https://tools.ssdc.asi.it/SED/

Table 5
Flux Calculation for Preflare (LS1) and Postflare (LS2) in Different Swift-UVOT Bands

Band	$\lambda_{\rm eff}$ (Å)	State	$M_{\rm obs}$	A_λ	$M_{\rm in}$	Zero Point	Flux (10^{-14} erg cm^{-2} s^{-1} Å^{-1})
v	5468	LS1	13.15 ± 0.02	0.06	13.09 ± 0.02	17.88 ± 0.01	40.94 ± 0.92
		LS2	13.15 ± 0.02		13.09 ± 0.03		40.94 ± 1.13
b	4392	LS1	14.13 ± 0.02	0.08	14.05 ± 0.04	18.98 ± 0.02	6.14 ± 0.20
		LS2	14.14 ± 0.02		14.06 ± 0.04		6.08 ± 0.19
u	3465	LS1	15.26 ± 0.02	0.10	15.16 ± 0.04	19.36 ± 0.02	1.55 ± 0.04
		LS2	15.35 ± 0.02		15.25 ± 0.04		1.43 ± 0.05
uvw1	2600	LS1	14.98 ± 0.02	0.13	14.85 ± 0.05	18.95 ± 0.03	3.02 ± 0.13
		LS2	16.52 ± 0.02		16.39 ± 0.05		0.73 ± 0.03
uvm2	2246	LS1	17.14 ± 0.03	0.18	16.96 ± 0.05	18.54 ± 0.03	0.63 ± 0.03
		LS2	15.44 ± 0.02		15.26 ± 0.05		3.02 ± 0.13
uvw2	1928	LS1	17.06 ± 0.02	0.16	16.90 ± 0.05	19.11 ± 0.03	0.39 ± 0.02
		LS2	17.06 ± 0.02		16.90 ± 0.05		0.39 ± 0.02

3. Multiwavelength SED Modeling

We constructed the MWSED by compiling the analyzed Fermi-LAT, Swift (see Sections 2.1 and 2.2), and the archived data (see Section 2.3), covering radio to gamma-ray frequencies. The MWSEDs corresponding to the low (combining LS1 and LS2) and flare states are shown in Figure 2 and Figure 3, respectively.

We consider a homogeneous spherical emission region of radius R' having a uniform magnetic field B' inside it, moving through a relativistic jet of bulk Lorentz factor Γ_b (corresponding to Doppler factor δ). This region contains relativistic electrons, which lose energy via synchrotron radiation and inverse-Compton (IC) processes. We are considering a leptonic model in which the energy loss of protons is insignificant compared to that of electrons.

As discussed in Section 2.1.1, from the ML analysis of Fermi-LAT data, a log-parabolic distribution of gamma rays was found to best fit the gamma-ray data of the flare and low states. A log-parabolic photon spectrum can be produced from the radiative loss of a log-parabolic electron spectrum (E. Massaro et al. 2004). Therefore, we have used a log-parabolic spectrum for the injected electrons in the emission region to explain the MWSED of M87, given by the following expression:

$$Q(E') = L_0\left(\frac{E'}{E'_0}\right)^{-\alpha-\beta\log_{10}\left(\frac{E'}{E'0}\right)}, \quad (3)$$

where $Q(E')$ is the log-parabolic distribution, L_0 is the normalization constant, E'_0 is the scaling factor or pivot energy (set to 1 TeV in our modeling and kept fixed), α is the spectral index, and β is the curvature index.

We use "GAMERA" (J. Hahn 2016), an open-source code to model the MWSEDs of M87, available on GitHub.[17] It solves the time-dependent transport equation (Equation (4)) and propagates the particle spectrum $N(E', t')$ for an injected spectrum to calculate the synchrotron and IC emissions, including the Klein–Nishina effect.

$$\frac{\partial N(E', t')}{\partial t'} = Q(E', t') - \frac{\partial}{\partial E'}(b(E', t')N(E', t')) - \frac{N(E', t')}{\tau'_{\rm esc}(E', t')}. \quad (4)$$

$Q(E', t')$ is the injected electron spectrum, and $b(E', t')$ corresponds to the energy loss rate by synchrotron and IC, and can be defined as $\left(\frac{dE'}{dt'}\right)$. In the last term, the escape timescale is assumed to be independent of energy and time, $\tau'_{\rm esc} = \eta'_{\rm esc}\frac{R'}{c}$, where $\eta'_{\rm esc}$ denotes the coefficient of escape time.

The code, subsequently, calculates the synchrotron and synchrotron self-Compton (SSC) emissions, which are Doppler boosted by a factor of δ^4 (C. D. Dermer & G. Menon 2009) in the observer's frame due to relativistic beaming, where $\delta = [\Gamma_b(1-\beta_j\cos\theta)]^{-1}$ is the Doppler factor, Γ_b is the bulk Lorentz factor, β_j is the intrinsic speed of the jet frame, and θ is the viewing angle of the jet with respect to the line of sight of the observer.

We have assumed two emission regions, one in the subparsec-scale jet and another in the kiloparsec-scale jet of M87. The light curve of the VHE flare data recorded by the LHAASO collaboration (Z. Cao et al. 2024) suggests a minimum variability timescale of 1 day, which constrains the size of the emission region. In our model, the VHE flare happened from the subparsec-scale jet; however, the kiloparsec-scale jet gives a dominant contribution to VHE gamma-ray data in the low state. In the subparsec-scale jet, the gamma rays are produced by the SSC mechanism, whereas in the kiloparsec-scale jet, they are mostly emitted by the external Compton mechanism (EC). In the EC mechanism, the external radiation fields provide the target photons for the IC scattering. The external radiation fields, e.g., cosmic microwave background (CMB), starlight, and the dust-emitted photons, are isotropic with respect to the AGN frame. The starlight and dust energy density of the host galaxy has been used from Ł. Stawarz et al. (2003) to calculate the EC emission from the kiloparsec jet of M87. The high-energy gamma rays produced in EC emission are Doppler-boosted by the factor of δ^6/Γ^2 in the observer's frame (C. D. Dermer & G. Menon 2009).

We have assumed the values of the physical parameters of the jets, for example, the magnetic field (G. Tomar et al. 2021) and the Lorentz factor (R. C. Walker et al. 2018; C.-C. Wang & H.-Y. Zhou 2009), following the earlier studies on the jets of M87.

The parameters listed in Tables 7 and 8 are adjusted to fit the simulated SEDs to the data points.

[17] http://libgamera.github.io/GAMERA/docs/main_page.html

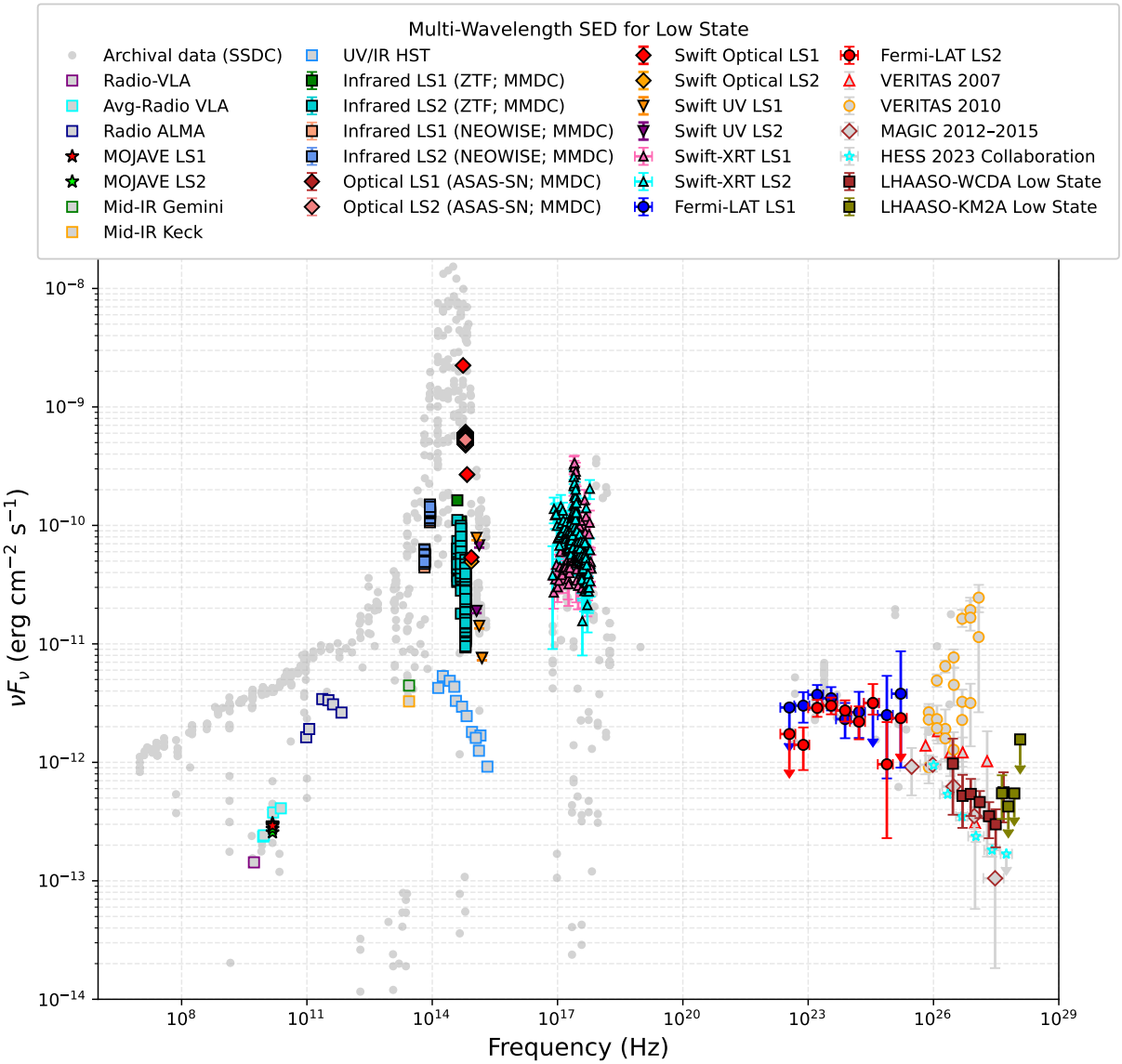


Figure 2. Multiwavelength SED plot for low state. Nonsimultaneous data points are represented by markers with solid gray and gray-filled colored edges, whereas simultaneous data points are represented by markers filled with one color and outlined with black color.

We used the following relation to determine the kinematic jet power of the flaring and low states in subparsec- and kiloparsec-scale jets, tabulated in Table 9:

$$P_{\rm tot} = \pi R'^2 \Gamma_b^2 c (U'_e + U'_B + U'_p). \quad (5)$$

The quantities in the AGN frame and the comoving jet frame are indicated by the unprimed and primed notations, respectively. U'_e, U'_B, and U'_p are the energy densities of electrons, magnetic field, and protons in the comoving jet frame. These are defined as follows:

$$U'_e = \frac{1}{V'} \int_{E'_{\rm min}}^{E'_{\rm max}} Q(E')\, E'\, dE', \quad (6)$$

where V is the volume of the emission region.

$$U'_B = \frac{B'^2}{8\pi}, \quad (7)$$

$$U'_p = n_p\, m_p\, c^2, \quad (8)$$

where m_p is the mass of a proton. We assumed that the number of protons (n_p) and radiating electrons is equal in the jet to maintain charge neutrality.

According to Event Horizon Telescope Collaboration (2019f), the estimated mass of the black hole ($M_{\rm BH}$) is $(6.5 \pm 0.7) \times 10^9\, M_\odot$ for an assumed distance of 16.8 Mpc; $M_\odot$ is the solar mass. Using this value, we calculated the Eddington luminosity $L_{\rm Edd} \approx 8.19 \times 10^{47}$ erg.sec^{-1}. The total kinematic jet power obtained in our model is less than the Eddington luminosity of M87.

4. Result: Multiwavelength Modeling

The LS1 and LS2 states were combined and labeled as the low state in this work. We modeled the MWSED of this state, with the SSC emission from the subparsec-scale jet. This model successfully explains the Fermi-LAT MeV–GeV observations as the Fermi-LAT data points are covered by the SSC bump. However, the SSC emission from the subparsec-scale jet is inadequate to account for the

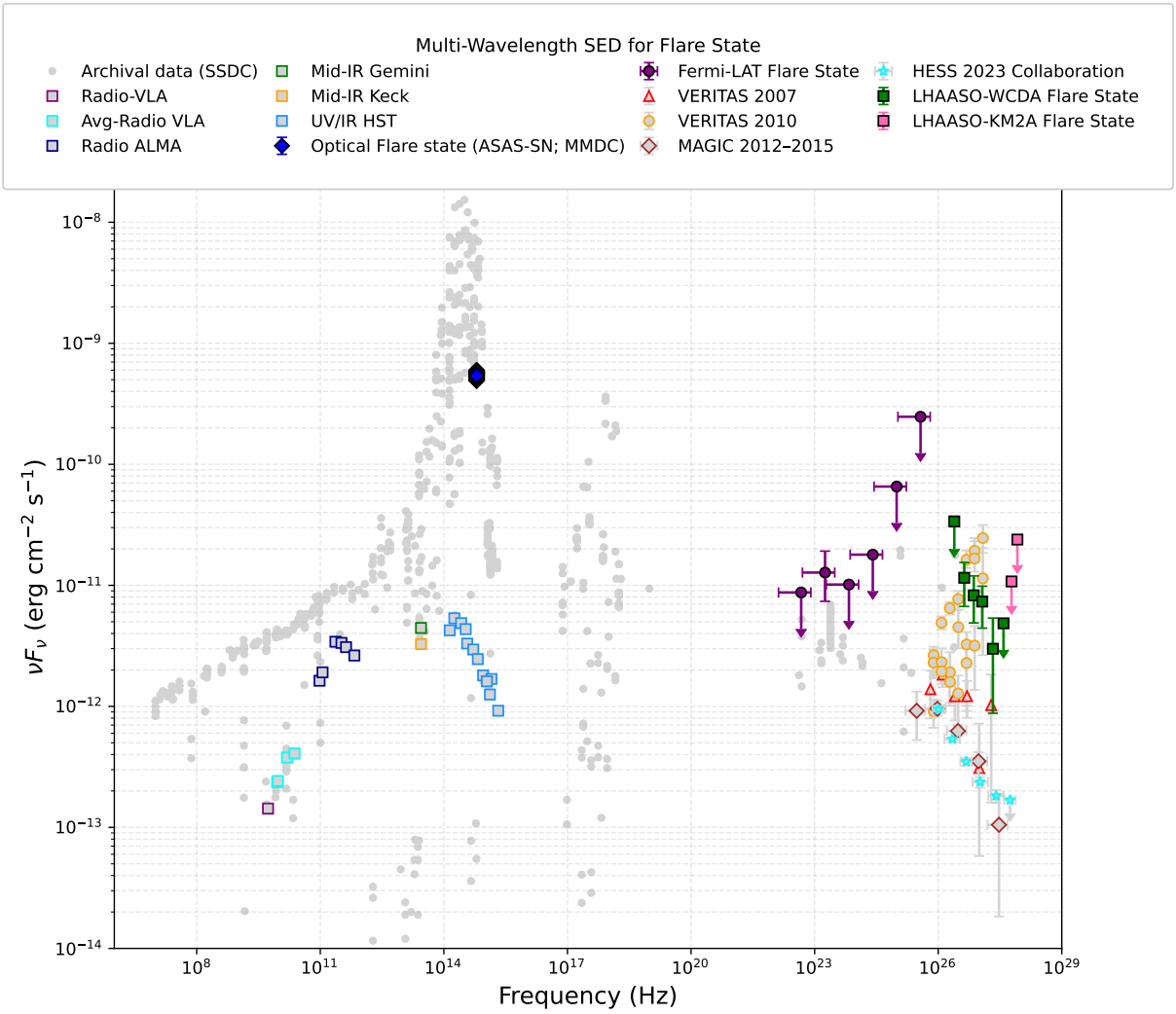


Figure 3. Multiwavelength SED plot for flare state. The marker style and color conventions are similar to Figure 2.

LHAASO-WCDA and LHAASO-KM2A data at higher energies (Figure 4); hence, we needed another emission region to explain the VHE gamma-ray emission. We considered the contribution from the kiloparsec-scale jet of M87 for this purpose. At the kiloparsec-scale jet, the EC emission is significantly higher compared to the SSC emission, as the emission region has a radius of the order of kiloparsecs ($\sim 10^{21}$ cm; H. E. S. S. Collaboration et al. 2020). The external photon fields, such as starlight, thermal dust emission, and the CMB, acted as targets for IC scattering. The corresponding energy densities of the external photon fields were adopted from Ł. Stawarz et al. (2003). The total emission from the kiloparsec-scale jet consists of the following components: synchrotron, SSC, IC/starlight, IC/CMB, and IC/dust. As shown in Figure 4, IC/starlight dominates and largely accounts for the observed TeV flux; the contribution from IC/CMB is lower than that of IC/starlight; and the contribution from IC/dust is lower than that of IC/CMB. The solid black curve in Figure 4 represents the total SED combining the subparsec and kiloparsec jets. The hardening of the VHE gamma-ray spectrum has been attributed to the EC emission from the kiloparsec-scale jet. The solid black curve passes through the first LHAASO-WCDA data point and the upper error bars of the subsequent LHAASO-WCDA data points. It also passes through the lower error bars of the LHAASO-WCDA and LHAASO-KM2A data points at the highest energy. Thus, our model is successful in explaining the complete gamma-ray spectrum covering the Fermi-LAT and LHAASO energy ranges. The model parameters are summarized in Table 7. The total resulting jet power, reported in Table 9, remained well below the Eddington limit of this source.

We modeled the flare-state MWSED with the SSC emission from the subparsec jet, as the light-curve analysis by the LHAASO collaboration already constrained the size of the emission region during the flare state. Figure 5 shows that the SSC model can explain the simultaneous GeV–TeV gamma-ray data. The solid black line, representing the total SED, touches the lower error bar of the Fermi-LAT data point, and it is below the Fermi-LAT upper limits. The LHAASO-WCDA data points shown with green colored boxes are well covered by the solid black line. The contribution from the kiloparsec-scale jet was also included, although it remained subdominant compared to the subparsec jet emission during the flare. The fitted parameters are provided in Table 8, and the powers of the individual components, along with the total power of the jet, are listed in Table 9. In this case also, the total jet power remained several orders of magnitude below the Eddington luminosity.

The low-energy data show sharp peaks, which are produced by host galaxy emission (M. Lucchini et al. 2019;

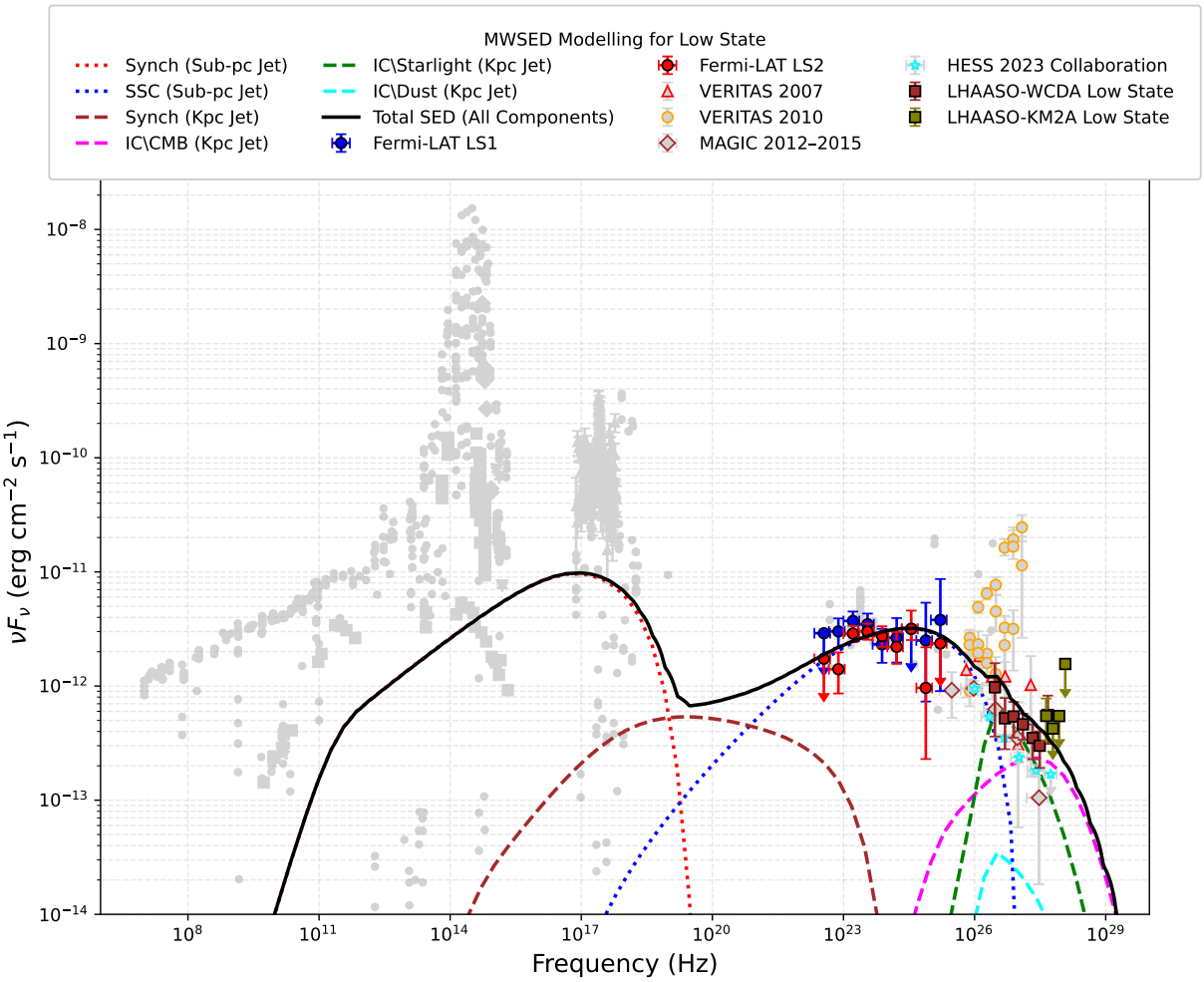


Figure 4. Multiwavelength (MW) modeling of the low state of M87 with contributions from the subparsec and kiloparsec-scale jets. SSDC data and host galaxy emission are shown in solid gray color. The red and blue dotted lines represent the synchrotron and SSC emission from the subparsec jet, respectively. The brown, magenta, green, and cyan dashed lines indicate the synchrotron, IC/CMB, IC/starlight, and IC/dust components in the kiloparsec jet. The sum of all of these components (total SED) is shown by the black solid line.

R. Xue et al. 2025). We have not fitted these peaks, as this work focuses on the jet emission and explains the origin of the VHE gamma rays detected from M87.

5. Discussion and Conclusion

Several emission models have been suggested previously to explain the MWSED of the M87 jet. A proton synchrotron model was discussed in this paper (A. Reimer et al. 2004). N. Fraija & A. Marinelli (2016) discussed photohadronic interactions to explain the VHE gamma-ray data of M87. In the paper by M. Boughelilba et al. (2022), the fitting of the SED involves different emission mechanisms that combine jet emission and accretion flow. The high-energy bump in the gamma-ray band is explained by proton synchrotron emission, and the X-ray energy band is attributed to the Comptonization of advection-dominated accretion flow photons. M. Lucchini et al. (2019) explained the radio-to-X-ray emission by a multizone model, which yields a lower gamma-ray flux than the measured flux. Two distinct one-zone leptonic models were employed in EHT MWL Science Working Group et al. (2021), but they failed to simultaneously represent the high- and low-energy components of the SED of M87. R. Alfaro et al. (2022) have shown that the one-zone SSC model, along with the photohadronic model, can explain the MWSED covering radio-to-VHE gamma-ray data. They included H.E.S.S., MAGIC, and HAWC data in their SED modeling. It is evident from their work that a separate emission model is needed to explain the VHE data of the M87 jet. The VHE gamma-ray data observed by the LHAASO collaboration show spectral hardening near 20 TeV, which has been explained by R. Xue et al. (2025) with the π^0 decay gamma rays produced in pp interactions, and also with the two-zone SSC model.

F. Ait Benkhali et al. (2019) argued that the one-zone SSC model is challenged by a potential excess over the standard power-law model at around 10 GeV during the low state of M87, which suggests the need for a second radiation component. The X-ray emissions from the knots in the kiloparsec scale of M87 have been studied earlier by reanalyzing the archival data from Chandra observations (X.-N. Sun et al. 2018). X.-N. Sun et al. (2018) modeled radio-to-X-ray data from the knots of the kiloparsec-scale jet of M87 with synchrotron emission of relativistic electrons. They noted that for some knots, a second component is needed to explain the high-energy data. G. Tomar et al. (2021) demonstrated that synchrotron and SSC emission from relativistic electrons in a subparsec-scale jet can account for the observed multiwavelength data from M87 up to 8 GeV. In

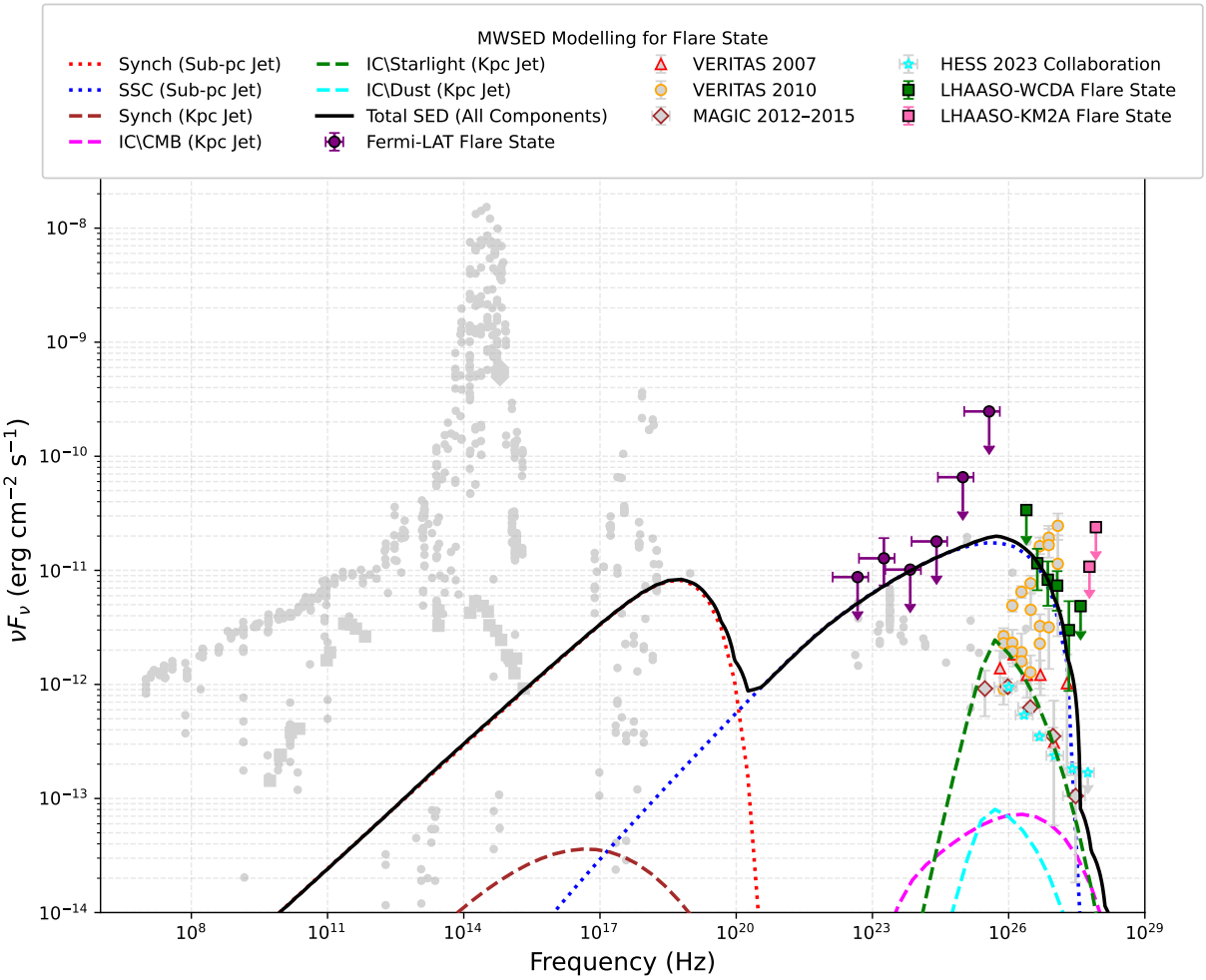


Figure 5. MW modeling of the flare state of M87 with contributions from the subparsec- and kiloparsec-scale jets. The line styles are similar to Figure 4. SSDC data and host galaxy emission are shown in solid gray color.

Table 6
Nonsimultaneous Observation Times for M87 Using Different Observing Facilities Spanning Various Energy Bands

Instrument	Start Time	End Time
Very Large Array (VLA; N. M. Nagar et al. 2001)	1999	...
Avg-VLA (M. A. Prieto et al. 2016)	2003-06	2004-12-31
Atacama Large Millimeter/submillimeter Array (M. A. Prieto et al. 2016)	2012-06-03	...
Keck I telescope (Long Wavelength Spectrometer; D. Whysong & R. Antonucci 2004)	2000-01-18	...
Gemini (E. S. Perlman et al. 2001)	2001-05	...
Hubble Space Telescope (HST; M. A. Prieto et al. 2016)	1998-01-16	2003-11-29
MAGIC (MAGIC Collaboration 2020)	2012	2015
Veritas (V. A. Acciari et al. 2008; E. Aliu et al. 2012)	2007-02	2007-04
	2010-04-05	2010-04-15
HESS (low state data in HESS collaboration 2023; F. Aharonian et al. 2023)	2004-02-16	2005-02-25
	2008-03-11	2009-03-21
	2012-10-31	2018-10-15

our work, we used a two-zone leptonic model to fit the broadband SED of M87; the two zones are located at the subparsec- and the kiloparsec-scale jets, respectively. In the low-state, the Fermi-LAT MeV–GeV data points are satisfactorily covered by the SSC emission from the subparsec-scale jet. LHAASO collaboration measured the emission of VHE gamma rays with a flux level of 10^{-12} erg cm^{-2} s^{-1} (Z. Cao et al. 2024) during this state. It was noted in their work that the low-state VHE emission has a higher possibility of coming from large-scale structures, such as the bright knots HST-1 and knot A in the kiloparsec-scale jet. We have shown that the LHAASO data points are well fitted by the VHE gamma-ray

Table 7
Results of Multiwavelength SED Modeling for Subparsec- and Kiloparsec-scale Jets in the Low State, Corresponding to Figure 4

Parameter	Symbol	Unit	Subparsec Jet	Kiloparsec Jet
Spectral index of injected electron spectrum	α	⋯	2.5	2.0
Curvature index of injected electron spectrum	β	⋯	0.019	0.021
Escape time coefficient	η'_{esc}	⋯	1	1
Magnetic field in emission region	B'	G	0.04	4×10^{-6}
Size of the emission region	R'	cm	1.8×10^{16}	1.8×10^{21}
Viewing angle	θ	deg	17°[a]	15°[b]
Doppler factor	δ	⋯	3.3[a]	2.29[b]
Lorentz factor	Γ_b	⋯	2.7[a]	1.45[b]
Min. Lorentz factor of injected electrons	$\gamma'_{\rm min}$	⋯	5.65×10^2	1×10^7
Max. Lorentz factor of injected electrons	$\gamma'_{\rm max}$	⋯	3.5×10^6	3×10^{11}
Starlight energy density	$U'_{\rm star}$	erg cm^{-3}	⋯	2.10×10^{-9}
Dust energy density	$U'_{\rm dust}$	erg cm^{-3}	⋯	2.10×10^{-11}
CMB energy density	$U'_{\rm CMB}$	erg cm^{-3}	⋯	8.76×10^{-13}

Notes.
[a] Adopted from R. C. Walker et al. (2018).
[b] Adopted from C.-C. Wang & H.-Y. Zhou (2009).

Table 8
Results of Multiwavelength SED Modeling for Subparsec- and Kiloparsec-scale Jets in the Flare State Corresponding to Figure 5

Parameter	Symbol	Unit	Subparsec Jet	Kiloparsec Jet
Spectral index of injected electron spectrum	α	⋯	2.29	2.21
Curvature index of injected electron spectrum	β	⋯	0.0019	0.17
Escape time coefficient	η'_{esc}	⋯	1	1
Magnetic field in emission region	B'	G	0.04	4×10^{-6}
Size of the emission region	R'	cm	1.5×10^{15}	1.8×10^{21}
Viewing angle	θ	deg	17[a]	15[b]
Doppler factor	δ	⋯	3.3[a]	2.29[b]
Lorentz factor	Γ_b	⋯	2.7[a]	1.45[b]
Min. Lorentz factor of injected electrons	$\gamma'_{\rm min}$	⋯	40	1.65×10^6
Max. Lorentz factor of injected electrons	$\gamma'_{\rm max}$	⋯	10.5×10^6	2.29×10^{11}
Starlight energy density	$U'_{\rm star}$	erg cm^{-3}	⋯	2.10×10^{-9}
Dust energy density	$U'_{\rm dust}$	erg cm^{-3}	⋯	2.10×10^{-11}
CMB energy density	$U'_{\rm CMB}$	erg cm^{-3}	⋯	8.76×10^{-13}

Notes.
[a] Adopted from R. C. Walker et al. (2018).
[b] Adopted from C.-C. Wang & H.-Y. Zhou (2009).

Table 9
Estimated Jet Power of Individual Components and Total Jet for Different States

State	Parameters	Subparsec Jet	Kiloparsec Jet	Total Jet Power ($P_{\rm tot}^{\rm sub\text{-}pc} + P_{\rm tot}^{\rm kpc}$)
Low State	Jet power of relativistic electrons (P_e)	1.60×10^{43} erg s^{-1}	1.56×10^{41} erg s^{-1}	3.20×10^{43} erg s^{-1}
	Jet power of magnetic field (P_B)	1.42×10^{40} erg s^{-1}	4.09×10^{41} erg s^{-1}	
	Jet power of cold protons (P_p)	1.55×10^{43} erg s^{-1}	4.01×10^{36} erg s^{-1}	
	Total kinematic jet power ($P_{\rm tot}$)	3.14×10^{43} erg s^{-1}	5.65×10^{41} erg s^{-1}	
Flare State	Jet power of relativistic electrons (P_e)	3.97×10^{43} erg s^{-1}	1.36×10^{41} erg s^{-1}	4.51×10^{44} erg s^{-1}
	Jet power of magnetic field (P_B)	9.84×10^{37} erg s^{-1}	4.09×10^{41} erg s^{-1}	
	Jet power of cold protons (P_p)	4.11×10^{44} erg s^{-1}	5.09×10^{37} erg s^{-1}	
	Total kinematic jet power ($P_{\rm tot}$)	4.50×10^{44} erg s^{-1}	5.45×10^{41} erg s^{-1}	

spectrum produced in EC emission of the ultrarelativistic electrons accelerated at the kiloparsec-scale jet of M87. This model can explain the hardening in the VHE gamma-ray spectrum near 20 TeV.

LHAASO collaboration (Z. Cao et al. 2024) also reported a flare in their VHE gamma-ray data, which lasted for 8 days in 2022. They observed that this flare rose fast ($\tau_{\rm d}^{\rm rise} = 1.05 \pm 0.49$ days) and decayed at a slower rate ($\tau_{\rm d}^{\rm decay} = 2.17 \pm 0.58$ days), and mentioned that its dayscale variability indicates that the VHE emission originates from a compact emission region that is only a few Schwarzschild radii from the center of the SMBH, with a radius of $R \sim 2.7 \times 10^{15}\,\delta\,$cm (Doppler factor $\delta \lesssim 3$). This implies that the acceleration and emission process of nonthermal particles may occur close to the central black hole. In earlier studies, the underlying physical mechanisms of such flares

have been speculated. According to recent high-resolution general relativistic magnetohydrodynamic simulations, flares close to the black hole event horizon may be powered by episodic magnetic reconnection events (B. Ripperda et al. 2020; H. Hakobyan et al. 2023). Another possible argument (M. V. Barkov et al. 2010; F. A. Aharonian et al. 2017) is that an efficient production of VHE photons through hadronic processes may result from interactions between a relativistic magnetized outflow near the jet formation zone and a star that was partially tidally disrupted by the contact with the SMBH. In our work, the SSC emission by the relativistic electrons in the subparsec-scale jet has been used to model the flare-state MWSED of M87 within a time-dependent framework; the GeV–TeV gamma-ray data are well explained by this model. The size of the emission region used in our model is comparable to that mentioned in the paper by the LHAASO collaboration (Z. Cao et al. 2024).

In conclusion, our two-zone leptonic model explains the flare and low-state data of LHAASO, the hardening in the LHAASO data in the low state, and the variability time in the flare state. Future observational data from LHAASO-WCDA and LHAASO-KM2A would be useful to understand more about the hardening in the spectrum of M87, as well as the measurement of the variability time from the gamma-ray light curve would be helpful to explore more about the location and size of the emission region.

6. Software and Third-party Data Repository Citations

The Fermi-LAT gamma-ray data analysis was done with "Fermipy" (M. Wood et al. 2017). Swift X-ray, ultraviolet, and optical data have been analyzed with "HEASoft" (NASA High Energy Astrophysics Science Archive Research Center Heasarc). We used data in our work from the MOJAVE database, which the MOJAVE team maintains (M. L. Lister et al. 2018), and data from SSDC and MMDC (D. Bégué et al. 2024; N. Sahakyan et al. 2024a, 2024b).

Acknowledgments

The data analysis for this work was performed using the computing facility at the Raman Research Institute. N.M. and S.K.M. thank A.K. Das for valuable discussions on X-ray data analysis. We thank the referee for many helpful comments.

Facilities: Fermi (LAT), Swift (XRT and UVOT).

Software: Fermipy (V1.0.1; https://fermipy.readthedocs.io/en/latest/; M. Wood et al. 2017), HEAsoft (V6.26.1; https://heasarc.gsfc.nasa.gov/docs/software/heasoft/; Nasa High Energy Astrophysics Science Archive Research Center (Heasarc) 2014), Xspec package (V12.14.1; K. A. Arnaud 1996), GAMERA (https://github.com/libgamera/GAMERA; J. Hahn 2016).

ORCID iDs

Nibedita Mondal https://orcid.org/0009-0009-8995-281X
Sandeep Kumar Mondal https://orcid.org/0000-0003-2445-9935
Nayantara Gupta https://orcid.org/0000-0002-1188-7503

References

Abdo, A. A., Ackermann, M., Ajello, M., et al. 2009, ApJ, 707, 55
Abramowski, A., Acero, F., Aharonian, F., et al. 2012, ApJ, 746, 151
Acciari, V. A., Beilicke, M., Blaylock, G., et al. 2008, ApJ, 679, 397
Acero, F., Ackermann, M., Ajello, M., et al. 2016, ApJS, 223, 26
Aharonian, F., Ait Benkhali, F., Arcaro, C., et al. 2023, A&A, 675, A138
Aharonian, F., Akhperjanian, A., Beilicke, M., et al. 2003, A&A, 403, L1
Aharonian, F., Akhperjanian, A. G., Bazer-Bachi, A. R., et al. 2006, Sci, 314, 1424
Aharonian, F., An, Q., Axikegu, et al. 2021, ChPhC, 45, 025002
Aharonian, F. A., Barkov, M. V., & Khangulyan, D. 2017, ApJ, 841, 61
Ait Benkhali, F., Chakraborty, N., & Rieger, F. M. 2019, A&A, 623, A2
Albert, A., Alvarez, C., Camacho, J. R. A., et al. 2021, ApJ, 907, 67
Albert, J., Aliu, E., Anderhub, H., et al. 2008, ApJ, 685, L23
Alfaro, R., Alvarez, C., Anita-Rangel, E., et al. 2025, ApJ, 994, 191
Alfaro, R., Alvarez, C., Arteaga-Velázquez, J. C., et al. 2022, ApJ, 934, 158
Algaba, J. C., Baloković, M., Chandra, S., et al. 2024, A&A, 692, A140
Aliu, E., Arlen, T., Aune, T., et al. 2012, ApJ, 746, 141
Arnaud, K. A. 1996, ASPC, 101, 17
Atwood, W. B., Abdo, A. A., Ackermann, M., et al. 2009, ApJ, 697, 1071
Ballet, J., Bruel, P., Burnett, T. H., Lott, B. & The Fermi-LAT collaboration 2023, arXiv:2307.12546
Barkov, M. V., Aharonian, F. A., & Bosch-Ramon, V. 2010, ApJ, 724, 1517
Bégué, D., Sahakyan, N., Dereli-Bégué, H., et al. 2024, ApJ, 963, 71
Bolton, J. G., Stanley, G. J., & Slee, O. B. 1949, Natur, 164, 101
Boughelilba, M., Reimer, A., & Merten, L. 2022, ApJ, 938, 79
Breeveld, A. A., Landsman, W., Holland, S. T., et al. 2011, AIPC, 1358, 373
Bruel, P., Burnett, T., Digel, S., et al. 2018, arXiv:1810.11394
Burrows, D. N., Hill, J. E., Nousek, J. A., et al. 2005, SSRv, 120, 165
Cao, Z. 2010, ChPhC, 34, 249
Cao, Z., Aharonian, F., Axikegu, et al. 2024, ApJL, 975, L44
Cappellari, M., Emsellem, E., Krajnović, D., et al. 2011, MNRAS, 413, 813
Connolly, S., McHardy, I., Skipper, C., & Emmanoulopoulos, D. 2016, MNRAS, 459, 3963
Cui, S., Liu, Y., Liu, Y., & Ma, X. 2014, APh, 54, 86
Dermer, C. D., & Menon, G. 2009, High Energy Radiation from Black Holes: Gamma Rays, Cosmic Rays, and Neutrinos (Princeton Univ. Press)
EHT MWL Science Working Group, Algaba, J. C., Anczarski, J., et al. 2021, ApJL, 911, L11
Event Horizon Telescope Collaboration 2019a, ApJL, 875, L1
Event Horizon Telescope Collaboration 2019b, ApJL, 875, L2
Event Horizon Telescope Collaboration 2019c, ApJL, 875, L3
Event Horizon Telescope Collaboration 2019d, ApJL, 875, L4
Event Horizon Telescope Collaboration 2019e, ApJL, 875, L5
Event Horizon Telescope Collaboration 2019f, ApJL, 875, L6
Fanaroff, B. L., & Riley, J. M. 1974, MNRAS, 167, 31P
Fermi Science Support Center 2025, Fermi LAT Data Server Query, https://fermi.gsfc.nasa.gov/cgi-bin/ssc/LAT/LATDataQuery.cgi
Fermipy Collaboration 2016, Fermipy Documentation (Latest Version), https://fermipy.readthedocs.io/en/latest/
Fitzpatrick, E. L. 1999, PASP, 111, 63
Fraija, N., & Marinelli, A. 2016, ApJ, 830, 81
H. E. S. S. Collaboration, Abdalla, H., Adam, R., et al. 2020, Natur, 582, 356
Hada, K., Asada, K., Nakamura, M., & Kino, M. 2024, A&ARv, 32, 5
Hahn, J. 2016, ICRC, 34, 917
Hakobyan, H., Ripperda, B., & Philippov, A. A. 2023, ApJL, 943, L29
Leahy, D. A., Foster, A., & Seitenzahl, I. 2024, AJ, 167, 130
Li, H.-C., Chen, M.-J., Jia, H.-Y., et al. 2014, ChPhC, 38, 016002
Lister, M. L., Aller, M. F., Aller, H. D., et al. 2018, ApJS, 234, 12
Lucchini, M., Krauß, F., & Markoff, S. 2019, MNRAS, 489, 1633
MAGIC Collaboration 2020, MNRAS, 492, 5354
Massaro, E., Perri, M., Giommi, P., & Nesci, R. 2004, A&A, 413, 489
Mills, B. Y. 1952, Natur, 170, 1063
MOJAVEWebpage 2016, https://www.cv.nrao.edu/MOJAVE/index.html
Mondal, S. K., Das, S., & Gupta, N. 2023, ApJ, 948, 75
Mondal, S. K., Prince, R., Gupta, N., & Das, A. K. 2021, ApJ, 922, 160
Nagar, N. M., Wilson, A. S., & Falcke, H. 2001, ApJ, 559, L87
Nasa High Energy Astrophysics Science Archive Research Center (Heasarc), 2014 HEAsoft: Unified Release of FTOOLS and XANADU, Astrophysics Source Code Library, ascl:1408.004
Perlman, E. S., Sparks, W. B., Radomski, J., et al. 2001, ApJL, 561, L51
Prieto, M. A., Fernández-Ontiveros, J. A., Markoff, S., Espada, D., & González-Martín, O. 2016, MNRAS, 457, 3801
Reimer, A., Protheroe, R. J., & Donea, A. C. 2004, A&A, 419, 89
Rieke, G. H., & Lebofsky, M. J. 1985, ApJ, 288, 618
Ripperda, B., Bacchini, F., & Philippov, A. A. 2020, ApJ, 900, 100
Roming, P. W., Kennedy, T. E., Mason, K. O., et al. 2005, SSRv, 120, 95
Sahakyan, N., Bégué, D., Casotto, A., et al. 2024b, ApJ, 971, 70
Sahakyan, N., Vardanyan, V., Giommi, P., et al. 2024a, AJ, 168, 289
Scargle, J. D., Norris, J. P., Jackson, B., & Chiang, J. 2013, arXiv:1304.2818
Schlafly, E. F., & Finkbeiner, D. P. 2011, ApJ, 737, 103
Schultz, G. V., & Wiemer, W. 1975, A&A, 43, 133

Stawarz, Ł., Sikora, M., & Ostrowski, M. 2003, ApJ, 597, 186
Sun, X.-N., Yang, R.-Z., Rieger, F. M., Liu, R.-Y., & Aharonian, F. 2018, A&A, 612, A106
Tomar, G., Gupta, N., & Prince, R. 2021, ApJ, 919, 137
Walker, R. C., Hardee, P. E., Davies, F. B., Ly, C., & Junor, W. 2018, ApJ, 855, 128
Wang, C.-C., & Zhou, H.-Y. 2009, MNRAS, 395, 301
Whittet, D. C. B., & van Breda, I. G. 1980, MNRAS, 192, 467
Whysong, D., & Antonucci, R. 2004, ApJ, 602, 116
Wood, M., Caputo, R., Charles, E., et al. 2017, ICRC, 35, 824
Xue, R., He, J.-C., Xiong, D., & Wang, Z.-R. 2025, ApJ, 990, 170
Zhang, S., Yang, M., Cao, Z., et al. 2020, ICRC, 36, 489